Biomaterials 33 (2012) 1079–1089

Contents lists available at SciVerse ScienceDirect

Biomaterials

journal homepage: www.elsevier.com/locate/biomaterials

Multifunctional nanoprobes for upconversion fluorescence, MR and CT trimodal imaging

Huaiyong Xing [a], Wenbo Bu [a,*], Shengjian Zhang [b], Xiangpeng Zheng [c], Ming Li [c], Feng Chen [a], Qianjun He [a], Liangping Zhou [b], Weijun Peng [b], Yanqing Hua [c], Jianlin Shi [a,*]

[a] State Key Laboratory of High Performance Ceramics and Superfine Microstructures, Shanghai Institute of Ceramics, Chinese Academy of Sciences, 1295 Ding-xi Road, Shanghai 200050, PR China
[b] Department of Radiology, Shanghai Cancer Hospital, Fudan University, Shanghai 200032, PR China
[c] Department of Radiation Oncology, Shanghai Huadong Hospital, Fudan University, Shangha, 200040, PR China

ARTICLE INFO

Article history:
Received 12 August 2011
Accepted 6 October 2011
Available online 5 November 2011

Keywords:
Multifunctional nanoprobes
Upconversion fluorescence
MRI
CT imaging
Surface plasmon resonance

ABSTRACT

Early diagnosis probes that combine fluorescence, X-ray computed tomography (CT) and magnetic resonance (MR) imagings are anticipated to give three dimensional (3D) details of tissues and cells of high resolution and sensitivity. However, how to combine these three modalities together within a sub-50 nm sized structure is technically challenging. Here we report a trimodal imaging probe of PEGylated NaY/GdF_4: Yb, Er, Tm @SiO_2-Au@PEG_{5000} nanopaticles of uniform size of less than 50 nm. The as-designed nanoprobes showed (1) strong emissions ranging from the visible (Vis) to near infrared (NIR) for fluorescent imaging, (2) T_1-weighted MRI by shorting T_1 relaxation time and (3) enhanced HU value as a CT contrast agent. The structure was optimized based on a comprehensive investigation on the influence of the distance between the NaY/GdF_4: Yb, Er, Tm core and Au nanoparticles (NPs) at the surface. The potential of trimodal imaging for cancerous cells and lesions was further demonstrated both *in vitro* and *in vivo*.

1. Introduction

In the past few years, significant attention has been focused on developing early cancer diagnosis using single or combined imaging modalities, such as optical [1,2], computed X-ray tomography (CT) [3], ultrasound [4], positron emission tomography (PET) [5] and magnetic resonance (MR) [1,2,5–8] imagings. Among them, CT is one of the most commonly used diagnostic tools, which could give high-resolution 3D structure details of tissues with differential X-ray absorption features. However, the clinically used CT contrast agents are problematic due to the use of iodinated compounds as contrast agent which are subject to short imaging time and even potential renal toxicity by their rapid kidney's clearance [9]. Several new CT contrast agents, such as Bi_2S_3, TaO_x and Au NPs were studied to overcome the shortages of iodine agents [10–13]. In comparison to traditional iodinated compounds, Au NPs, which have low toxicity and long imaging time, possess a higher absorption coefficient than iodine (e.g., at 100 keV: gold: 5.16 $cm^2\ g^{-1}$; iodine: 1.94 $cm^2\ g^{-1}$) [14]. More importantly, fluorescent enhancement effect due to the surface enhanced Raman scattering (SERS) of Au NPs has been well-documented and widely used for fluorescent imaging [15–17]. Although CT technique could provide relatively high resolution image, its clinical application has been limited largely because of the low sensitivity (especially to the soft tissues with limited density differences). Fortunately, MRI has lower resolution but higher sensitivity to soft tissues than CT imaging for non-ionizing radiation. Therefore it is believed that the combination of CT imaging with MRI modality might show a greater probability to improve the quality of the tissue imaging. Gadolinium chelate-coated Au NPs as a contrast agent for CT and MRI has been reported, but gadolinium was chelated outside, leading to the possible Gd^{3+} leaking problem [18]. Water-soluble FePt alloy NPs were also investigated for possible CT/MR dual imaging, however the signals for bimodal imaging were rather weak [19].

In spite of the advantages of the CT and MRI, these two imaging modalities share the same shortage: unable of cellular imaging and therefore no cell-level information can be acquired. Optical imaging, on the other hand, has high resolution and sensitivity for imaging at the cellular level but could not provide spatial resolution and 3D tissue detail [1,20]. If the cellular-sensitive fluorescent imaging can be combined together with CT and MR imagings, high resolutional/

* Corresponding authors. Tel.: +86 21 52412714; fax: +86 21 52413122.
E-mail addresses: wbbu@mail.sic.ac.cn (W. Bu), jlshi@sunm.shcnc.ac.cn (J. Shi).

0142-9612/$ – see front matter © 2011 Elsevier Ltd. All rights reserved.
doi:10.1016/j.biomaterials.2011.10.039

sensitive imagings of both tissues and cells could be obtained. Former paramagnetic CdS: Mn/ZnS quantum dots (QDs) were reported as multifunctional probes for optical, CT and MR imagings [21]. However, the inherent toxicity [22,23] of QDs limited their further application as imaging probes. The commonly used fluorescent probes, such as organic dyes and QDs, are excited by ultraviolet (UV) light which is harmful and almost non-penetrable to tissues. In contrast, NIR-excited UCNPs have been known as low toxic and stable fluorescent probes for their deep tissue penetration with greatly reduced photodamage and auto-fluorescence [24,25]. Among them, hexagonal-phase $NaYF_4$ has been demonstrated as an efficient upconversion host material for strong fluorescence under 980 nm laser excitation [26]. In our previous research, we used Fe_3O_4/$NaYF_4$: Yb, Er fluorescent bimodal probes for combined MR and optical imaging, but fluorescent quenching happened inevitably due to the existence of black Fe_3O_4 [27]. Recently Li and coworkers reported an interesting core–shell $NaYF_4$:Yb^{3+},Tm^{3+}@Fe_xO_y nanostructure for dual-modality T_2-enhanced MR and NIR-to-NIR upconversion luminescent imagings, however, luminescence quenching effect was still present due to the Fe_xO_y shell [28]. On the contrary, gadolinium as a positive T_1-weighted MRI contrast agent [29–31] can form homogeneous Gd-Y solid solution in rare earth (RE) fluoride ($NaREF_4$). Recently, Gd^{3+}–RE^{3+} codoping in UCNP has been demonstrated favorable for the phase transition from the cubic to hexagonal and highly luminescent at appropriate dopant concentrations [32]. In addition to affecting the luminescence, Gd^{3+} doping in UCNP was also demonstrated feasible in T_1-weighted MR imaging, and thus provided a platform for simultaneous MR and optical imaging [33–35]. Based this platform, several interesting studies for combining MR, fluorescence and PET imaging have been reported very recently [36,37]. However, how to combine the MR and optical imaging platform with CT imaging function without sacrificing their individual functions remains a big challenge.

Herein, we report the combination of Gd–RE doped UCNPs with Au NPs based on a simple electrostatic adsorption mechanism between positively charged UCNP@SiO_2–NH_2 and negatively charged Au NPs, resulting in a sub-50 nm sized multifunctional nanostructure with trimodal imaging modalities. Detailed investigations were carried out to perfect the trimodal imaging property of the as-designed probe. Gadolinium ions and gold NPs act as MR and CT imaging contrast agents respectively. The as-prepared UCNP (hexagonal phase NaY/GdF_4: Yb, Er, Tm) was spherically shaped of 25–26 nm in diameter and emitted strong lights ranging from Vis to NIR under 980 nm laser excitation. Here, the interesting NIR excitation/emission feature combines the merits of deep penetration and less auto-fluorescence in tissues, being expected to enhance the signal-to-noise ratio (SNR) [35,38,39].

As the UCNPs were hydrophobic, a W/O microemulsion method was used to coat a water-soluble silica shell onto the surface of UCNPs to enhance the hydrophility of the biomarker and reduce the toxicity of the UCNPs [40,41]. With the amino-ends on the outside, gold NPs were attached on the silica shell by electrostatic adherence. PEG outer layer with good biocompatibility was then coated to enhance the dispersity of the nanoprobes in PBS buffer. The PEGylation could be further adopted to prevent the quick clearance by the reticuloendothelial system (RES) which could enhance the dose delivery efficiency in tumor *via* the EPR effect [42–44]. In previous reports, gold NPs have been investigated to enhance the fluorescent emission of UCNP through the surface plasmon resonance (SPR) effect [45,46]. Here, the distance between the noble metal and fluorescent probe is expected to play an important role in SPR effect. Although the distance between gold NPs and QDs has been known to be important for strong luminescence [17,47–49], it has not been optimized between UCNP and gold NPs. As the thickness of silica shell could be feasibly tuned, the distance between UCNP and gold NPs in our structure could be easily changed, and therefore the optimized shell thickness and the effect of gold content would be well determined. Notably, this work combined the functions of upconversion fluorescent, MR and CT bioimagings into one system, and the feasibility of the probe both *in vitro* and *in vivo* were investigated.

2. Experimental

2.1. Materials

Tetrakis-hydroxymethyl-phosphonium chloride (THPC, 80%), Rare earth chlorides (99.9%), 3-Aminopropyl-triethoxysilane (APTS, 99%), O-[2-(3-Mercaptopropionylamino) ethyl]-O′-methyl-polyethyleneglycol (PEG_{5000}–SH), 1-Octadecene (90%), Ninhydrin (2, 2-Dihydroxyindane-1, 3-dione), Igepal CO-520 (NP-5) were purchased from Sigma–Aldrich. Oleic acid (OA), TEOS, NaOH, NH_4F, CH_3OH and CH_3CH_2OH were obtained from Shanghai Lingfeng Chemical Reagent Co., LTD. and $HAuCl_4$, ammonia solution (30%) were from Sinopharm Chemical Reagent Co., LTD. All reagents were of analytical grade and used without any purification. Deionized water was used throughout.

2.2. Synthesis of multifunctional nanoprobes

2.2.1. Synthesis of β-NaY/GdF_4: Yb, Er, Tm (UCNP) nanocrystals

The spherical upconversional NaY/Gd(15%)F_4: Yb (20%), Er(2%), Tm(0.5%) nanoparticles were prepared according to the literature [50]. In a typical procedure, 1 mmol of $RECl_3$ (RE = 62.5%Y, 15%Gd, 20%Yb, 2%Er and 0.5%Tm) powder was dissolved in 100 mL flask containing 4 mL of water. 6 mL of oleic acid and 15 mL 1-octadecene were then added into flask and mixed for several minutes. The solution was heated to 160 °C for 1 h to remove the excess water and then cooled down to room temperature. Subsequently, methanol solution of NH_4F and NaOH was added into the solution and stirred for 1 h. After the evaporation of methanol, the solution was slowly heated to 300 °C and maintained for 1.5 h under the protection of argon to obtain the hydrophobic nanocrystals. The product was washed with ethanol several times and finally dispersed in cyclohexane.

2.2.2. Synthesis of single-loaded UCNP@SiO_2-NH_2

In a typical procedure [41], 1 mL of Igepal CO-520 (NP-5) was dispersed in 20 mL of cyclohexane. Afterwards, 0.15 mmol UCNP-cyclohexane solution was injected into the mixture. After magnetic stirring for 3 h, 1.5 mL of ammonia (30%) was added. Using a Syringe Pump to control the adding rate, 0.1, 0.2, 0.3 and 0.5 mL of TEOS was added respectively into the system to get controllable thickness of silica: 5 nm, 10 nm, 15 nm and 20 nm, respectively. The mixture was sealed and kept stirring for 24 h. To graft amino-groups, 50 μL APTES was injected into the system and kept stirring for 4 h. Methanol was then added to precipitate the product. Collected by centrifugation, washed with ethanol several times, the product was finally dispersed in deionized water.

2.2.3. Synthesis of Au NPs and their attachment on UCNP@SiO_2-NH_2

1–2 nm Au nanoparticles were prepared using THPC as reductant according to Duff et al. [51] and aged two weeks for future use. Mixing UCNP@SiO_2-NH_2 with Au NPs solutions together, the Au NPs could be attached onto the silica surface after 20 min of ultrasonication. Adding different amounts of Au NPs, UCNP@SiO_2–Au NPs of different ratio of Au/UCNP can be obtained. 5 mg PSG_{5000}–SH was added and the solution was then ultrasonicated for 10 min. The PEG modified composite NPs were then centrifuged

and washed with water for three times. Upconversional sesame balls (UCS-Balls) were finally obtained.

2.3. Characterization

X-ray powder diffraction (XRD) measurements were performed on a Rigaku D/MAX-2250 V diffractometer with graphite-monochromatized Cu Kα radiation. The morphology and Energy-dispersive X-ray analysis (EDXA) of the nanocrystals were performed on a JEOL 200CX microscope operated at 200 kV. Fourier transform infrared spectroscopy (FT–IR) spectra were recorded on a Nicolet 7000-C spectrometer by using pressed KBr tablets. Upconversion luminescence emission spectra were collected on Fluorolog-3 Spectrofluorometer (Jobin Yvon, France), with the excitation of a 450 W xenon lamp and an external 0–1 W adjustable 980 nm semiconductor laser (Beijing Hi-tech Optoelectronic Co., China). Dynamic light scattering (DLS) and zeta potential analysis was performed on Nano-Zetesizer (Malvern Instruments Ltd).

2.4. Cell culture

MCF-7 cells were cultured at 37 °C and with 5% CO_2 in Roswell Park Memorial Institute medium (RPMI) 1640 supplemented with 10% fetal bovine serum (FBS) and 1% penicillin/streptomycin.

2.5. Cell cytotoxicity assessment

The cell cytotoxicity *in vitro* was measured using 3-(4, 5-dimethylthiazol-2-yl)-2, 5-diphenyltetrazolium bromide (MTT) assay. MCF-7 cells were seeded into a 96-well cell-culture plate at 10^6/well and then incubated for 24 h at 37 °C under 5% CO_2. RPMI 1640 solutions of UCS-Balls with different concentrations of 6.25, 12.5, 25, 50, 100, 200, 400 and 800 μg/mL were added to the wells. The cells were then incubated for 6 or 24 h at 37 °C under 5% CO_2. The cell viability was then calculated by MTT assy.

2.6. Confocal fluorescence imaging

800 μg/mL UCS-Balls were incubated with MCF-7 (10^6/well) for 0, 0.5, 2, 6 and 12 h at 37 °C under 5% CO_2. After washed with PBS for three times, the nuclei were stained with 1–2 μg/mL 4′-6-Diamidino-2-phenylindole (DAPI) for 15 min. After washed with PBS again for three times, confocal fluorescence imaging of cells was acquired with a Olympus FV1000 laser-scanning microscope equipped with a CW NIR laser at λ = 980 nm as the excitation source, while DAPI was excited with 359 nm light. A 60 × oil-immersion objective lens was used and luminescence signals were detected in the wavelength regions of 500–560 nm and 620–680 nm.

2.7. MR and CT imaging in vitro

0, 400 and 800 μg/mL UCS-Balls were incubated with MCF-7 (10^6/well) for 12 h at 37 °C under 5% CO_2. After washing with PBS for three times, MCF-7 containing UCS-Balls in PBS were precipitated at the bottom of the tube after centrifugation. The MR imaging experiments were performed on a 3.0-T clinical MRI instrument (GE Signa 3.0T), and the pulse sequence used was a T_1-weighted FSE-XL/90 sequence with the following parameters: TR/TE = 1000, 2000, 3000, 4000/7.9 ms: field of view [FOV]: 18 cm^2; matrix: 128 × 128; number of excitations (NEX): 2; slice thickness = 2 mm; space = 0.5 mm; FOV: 18 cm; coil: QUADKNEE. The CT tests were performed on GE discovery CT750 HD, GE Healthcare, WI with 5 mm slice thickness and 5 mm interval at 120 kVp and 100 mAs with the following parameters: beam collimation, 64 × 0.625 mm; table speed, 27 mm per rotation; beam pitch, 1.25; gantry rotation time, 1.0 s.

2.8. Tumor xenograft and trimodal imaging in vivo

Animal procedures were in agreement with the guidelines of the Institutional Animal Care and Use Committee. Walker 256 cells (5 × 10^6 cell/site) were implanted subcutaneously into SD mice. Trimodal imaging studies were performed when tumor reached 10–12 mm in average diameter (3 weeks after implant). *In vivo* MR/CT imaging was performed in 5 min after the injection of 200 μL UCS-Balls PBS (dose: 303.2 μg Gd kg^{-1}, 1.087 mg Au kg^{-1}), on a 3.0 T clinical MRI instrument (GE Signa 3.0T)/GE discovery CT750 HD, GE Healthcare.

3. Results and discussion

3.1. Synthesis and characterization of multifunctional nanoprobes

The synthetic process for mutifunctional probes was illustrated in Fig. 1A. Typically, the as-prepared hydrophobic UCNPs were coated with a thickness-controllable silica shell in the water–in–oil (W/O) reverse microemulsion system [27,41]. After the surface modification using well-established silica chemistry, the outer surface of UCNP@SiO_2 was modified with amino-groups using 3-aminopropyl triethoxysilane (APTS) to obtain UCNP@SiO_2-NH_2 with positively charged surface. Then the as-prepared negatively charged Au NPs were well-attached onto the surface of silica based on electrostatic attraction. Finally, to ensure high stability of the probe in biological media (such as PBS buffer and normal saline) and also prolong blood circulation time in live system, PEG_{5000}–SH was selected and grafted onto the surface of the probes. The final structure looks like a Chinese sesame ball: The small Au NPs are the sesame seeds well-distributed around the silica shell surface and UCNP core is the inner filling. The final product is named as upconversional sesame ball (UCS-Ball).

3.1.1. Synthesis and characterization of UCNPs

Gd^{3+}-doped UCNPs were prepared using a literature-reported thermal decomposition method with slight modification [50]. The as-prepared NaY/GdF_4: Yb, Er, Tm-UCNPs were characterized by X-ray powder diffraction (XRD, Fig. S1A) which clearly shows the patterns of a hexagonal phase (Standard PDF card: 16-0334) without detectable signals of the cubic phase. The NPs are highly crystalline without any impurity phase existing. As shown in Fig. 1B and S1B, all the obtained UCNPs show narrow size distribution and high shape uniformity. These small nanocrystals are spherically shaped with an average size of *ca.* 25 nm. The HR-TEM image (Fig. S1C) and selected area electron diffraction (SAED) pattern (Fig. S1D) of a single UCNP give more detailed structural information and show single-crystallinity of the product. The energy dispersive X-ray (EDX) spectrum (Fig. S1E) shows that all the elements (Na, Y, F, Er, Yb, Tm, Gd) are included in the co-doped NPs. The emission spectrum under continuous wave (CW) laser excitation at 980 nm for β-NaY/GdF_4: Yb, Er, Tm is illustrated in Fig. 2, showing wide emission bands ranging from Vis to NIR. The emission peaks at 519, 538, and 652 nm are assigned to the transitions from energy levels $^2H_{11/2}$, $^4S_{3/2}$ and $^4F_{9/2}$ to $^4I_{15/2}$ of Er^{3+}, respectively. The emission peaks at 693 and 800 nm are due to transitions from $^3F_2$, $^3F_4$ to $^3H_6$ of Tm^{3+}, respectively. These green (*ca.* 519, 538 nm) and red (*ca.* 652, 693 nm) emissions could be discerned by naked eyes and captured using digital camera, as shown in the inset in Fig. 2. It is worthy to mention that the emission intensity of the NIR (800 nm) band is much stronger than any other emission bands, showing great potential in biological imaging with expected deep penetration [35,38].

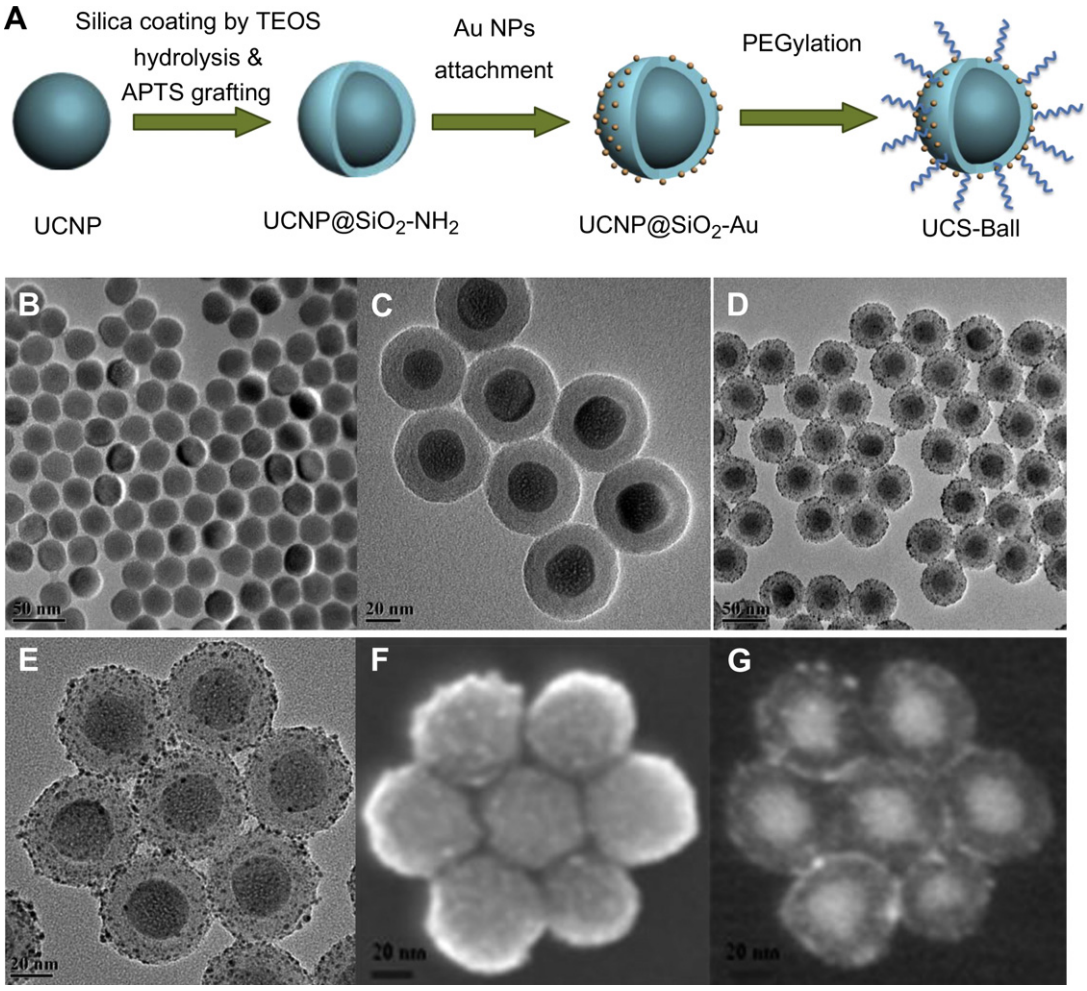

Fig. 1. Schematic illustration for the synthesis of UCS-Balls (A); TEM images of UCNPs (B), UCNP@SiO_2 (C), UCS-Balls (D and E); Backscattered morphological and compositional SEM images of UCS-Balls (F and G, respectively).

3.1.2. Synthesis and characterization of UCNP@SiO_2-NH_2

As the oleic acid coated UCNPs were hydrophobic, water-soluble silica shell was coated to make the UCNPs hydrophilic. Well-established water–in–oil (W/O) reverse microemulsion method was used in this work [52]. APTS was added *in situ* to modify silica shell with amino-groups for obtaining a positively charged surface, which was a widely used procedure in silica chemistry. As-synthesized UCNP@SiO_2-NH_2 core–shell single-loaded structure could be clearly seen in Fig. 1C. The thickness of the silica shell was estimated to be *ca.* 10 nm, and could be facilely tuned by changing the adding amount of TEOS precursor. The NPs showed excellent dispersion in water (Fig. 3A), and their surface charge was about +11.7 mV (Fig. 3C) tested by Zetasizer. Another evidence for the successful modification of silica surface with amino-groups was the color change, from the colorless to purple (Fig. 3B), after using a convenient ninhydrin reaction [53].

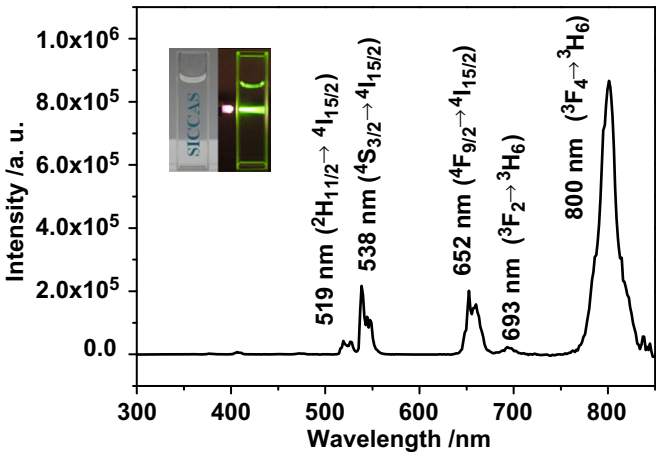

Fig. 2. Emission spectra of 1 wt% hexamethylene solutions of NaY/Gd (15%)F_4: Yb (20%), Er (2%), Tm (0.5%), Inset picture was a photo showing the upconversion luminescence excited by 980 nm laser (1W).

3.1.3. Synthesis and characterization of UCS-Balls

Electrostatic attraction is a simple but effective way to bridge two oppositely charged subjects [54,55], which was used in our system for Au NPs decoration. Negatively charged Au NPs with an average size of 2 nm (Fig. S2) were prepared using previously reported method [51]. By electrostatic adhesion, Au NPs could be easily attached onto the surface of UCNP@SiO_2-NH_2. Afterwards, PEG_{5000}–SH was coated on the Au NPs by the formation of the Au–S bond, leading to the final PEGylated Au NPs decorated core–shell nanostructure as shown in TEM (Fig. 1D,E) and SEM (Fig. 1F,G) images. The zeta potential of UCS-Balls (Fig. 3H) changed from the positive (+11.7 mV) to negative (−16.9 mV) after Au NPs decoration, which is another evidence of successful surface modification. Dynamic light scattering (DLS) analysis (Fig. 3J) of UCS-

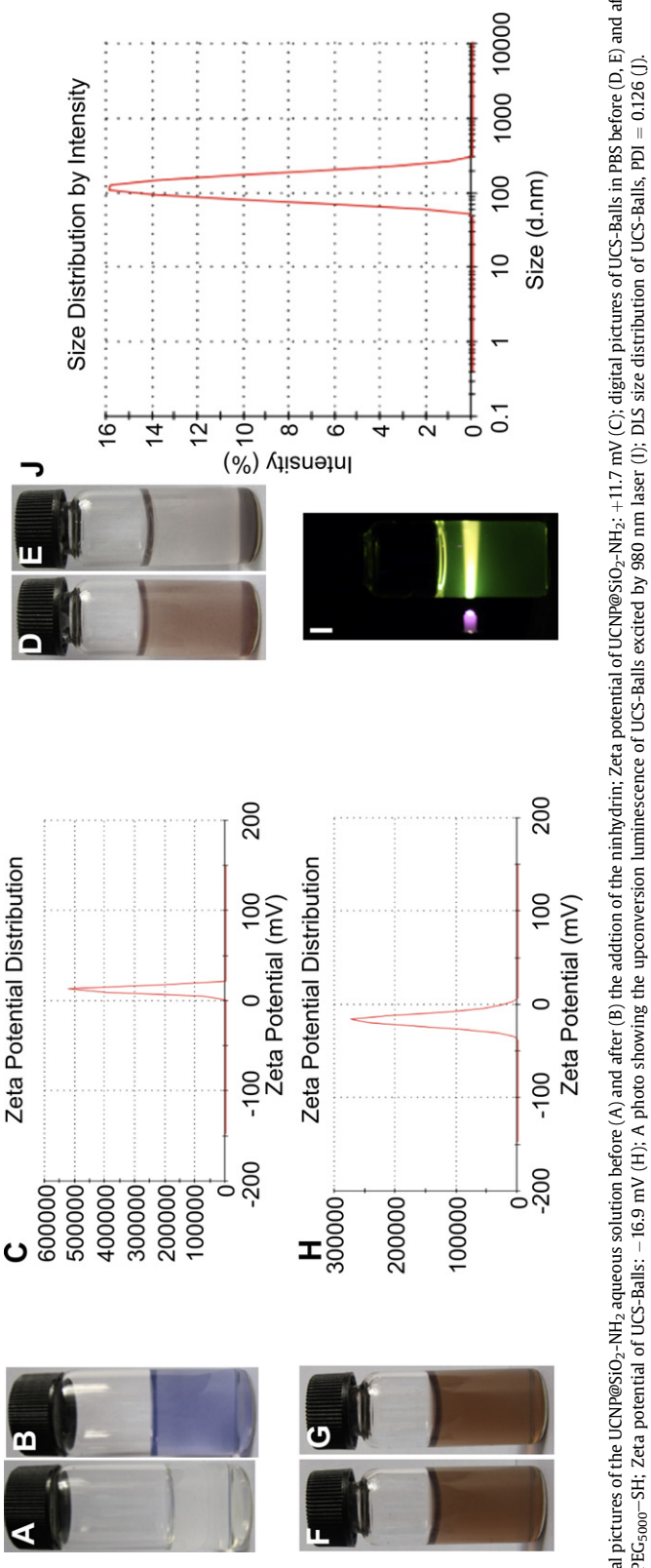

Fig. 3. Digital pictures of the UCNP@SiO_2-NH_2 aqueous solution before (A) and after (B) the addtion of the ninhydrin; Zeta potential of UCNP@SiO_2-NH_2: +11.7 mV (C); digital pictures of UCS-Balls in PBS before (D, E) and after (F, G) the addition of PEG_{5000}–SH; Zeta potential of UCS-Balls: − 16.9 mV (H); A photo showing the upconversion luminescence of UCS-Balls excited by 980 nm laser (I); DLS size distribution of UCS-Balls, PDI = 0.126 (J).

Balls shows an average diameter of 112.9 nm and a low polydispersion index (PDI) of 0.126, indicating that UCS-Balls are perfectly monodispersed in water. It is well known that, silica or silica shielded nanoparticles can hardly be dispersed in PBS buffer (Fig. 3D) and are very likely to precipitate within a few minutes (Fig. 3E). Here, by surface modification using PEG_{5000}, Fig. 3F shows the greatly improved stability of UCS-Balls dispersion in PBS buffer. No noticeable sedimentation can be observed even after storage over three weeks (Fig. 3G). As shown in Fig. 3I, UCS-Balls emit strong yellow green light under 980 nm laser excitation, which could be promising fluorescent probes.

The size of Au NPs was one of the key parameters for the successful attachment onto the silica surface and overlarge Au NPs would exhibit much weaker electrostatic adhesion [56]. Therefore, negatively charged Au NPs with an average of 2 nm are used. The UV–Vis absorption spectrum of the Au NPs shows no distinct absorption at around 550 nm (Fig. 4A). When these Au NPs are loaded onto UCNP@SiO_2-NH_2, a weak absorption band in the green light region can be observed, indicating slight aggregation among NPs. Fourier transform infrared spectroscopy (FT–IR) was used to further demonstrate the sequential surface modification starting from hydrophobic UCNPs (Fig. 4B). Oleic acid (OA) was used as surfactant on the surface of UCNPs to stabilize the solution and prevent aggregation. As shown in Fig. 4B, the broad band at 3448 cm^{-1} can be assigned to the stretching vibration of the O–H (COOH); the 2926 and 2855 cm^{-1} bands are assigned to the stretching vibration of methylene (CH_2) in the oleic acid molecules, the bands at 1569 and 1459 cm^{-1} are for the stretching vibration of the carboxylic group (C=O). After SiO_2 coating, the Si–O–Si asymmetric stretching ($\sim$1088 cm^{-1}) and deformation (797 and 463 cm^{-1}) vibrations can be observed. After the APTS modification, the SiO_2 shell bears NH_2-ends on its outer surface, therefore, the 3423 and 1637 cm^{-1} band are attributed to the stretching and bending vibrations and of N–H. The characteristic bands of SiO_2 become weaker after the PEGylation. The grafted PEG_{5000}–SH (*o*-[2-(3-Mercaptopropionylamino) ethyl] - *o*′-methylpolyethylene glycol) has N–H, C–H and H_2C–O bonds, and all these IR characteristic bands can be detected in Fig. 4B: 3431 and 1637 cm^{-1} bands corresponding to stretching and bending vibrations of N–H, 2891 cm^{-1} band to the stretching vibration of the CH_2 and CH_3. The stretching vibration of C–O–C was overlapped with the wide Si–O–Si asymmetric stretching vibration band at 1088 cm^{-1}.

3.2. Effect of the distance between UCNP core and gold NPs and Au content on the SPR effect

3.2.1. Effect of the distance

Surface plasmon resonance effect is resulted from the interaction between luminescence and collective oscillations of free electrons on metallic surfaces [16,57]. The radiative decay rates and emission of optical probes could be enhanced by the SPR effect. Recently, fluorescence enhancement of UCNPs by direct attachment of Au NPs has been reported, where the particle sizes were too large (*ca.* 200 nm in diameter) to be applied for biological imaging [45,46]. It is believed that the distance between UCNPs and metallic NPs should play an important role in the SPR effect, but such investigation has never been reported. Here, we were able to precisely tune the distance between inner UCNP core and outer Au NPs *via* changing the thicknesses of silica protective shell simply by using varied TEOS amount. As seen in Fig. 5A–D, UCS-Balls with varied UCNP-Au distance, ranging from 5 to 20 nm, were successfully synthesized. The loading amount of Au NPs was carefully controlled with a constant Y/Au ratio of about 0.8. From the emission spectra of UCS-Balls of different distances (d) between Au NPs and UCNP (e.g. $d = 5, 10, 15$ and 20 nm in Fig. 5), we could conclude

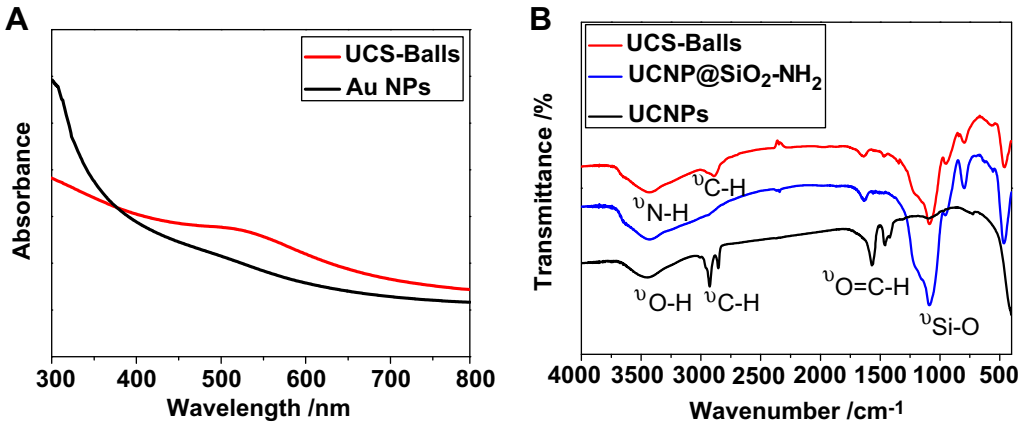

Fig. 4. A) UV–Vis absorption spectra of Au NPs (black line) and UCS-Balls (red line); B) FT-IR spectra of UCNP (black line), UCNP@SiO_2-NH_2 (blue line), UCS-Balls (red line).(For interpretation of the references to colour in this figure legend, the reader is referred to the web version of this article.)

that the fluorescence reaches a maximum at $d = 10–15$ nm for the SPR effect. When Au NPs and UCNP were closer to each other (e.g. $d = 5$ nm), the fluorescence intensity dropped nearly by a factor of 1.7 relative to the maximum ($d = 10, 15$ nm). This observation was similar to the reports about quenching of photoluminescence (PL) between gold and QDs at very short inter-particle distances [47–49]. Our investigations suggested that, when the distance was less than *ca.* 5 nm, the quenching of PL became more significant possibly due to the dominance of resonant energy transfer (RET) in the UCNP/Au system. However, with the distance increased to 20 nm, much decreased PL intensity can also be seen, indicating the greatly suppressed SPR effect from Au NPs. Therefore, a silica shell thickness of 10–15 nm might be the optimum distance between UCNP and Au NPs for enhanced SPR effect. Hence, in the following work, a silica shell thickness of 10 nm was chosen for the preparation of UCS-Balls.

3.2.2. *Effect of the Au loading content*

Previous reports have already shown the influence of Au loading on the optical property of NPs, but no optimal Au loading content for PL was obtained [58,59]. The mechanism for the enhancing/quenching of PL is not clear yet. Huang's recent research showed that emission intensity of UCNPs increased with the increase of the number of attached Au NPs [45], while proximal Au NPs were found to quench the photoluminescence of the semiconductor quantum dots [49]. Here, efforts are made to find the dependence manner of PL intensity on Au content in the UCS-Balls and its potential PL enhancing/quenching mechanism. UCS-Balls with different Au/

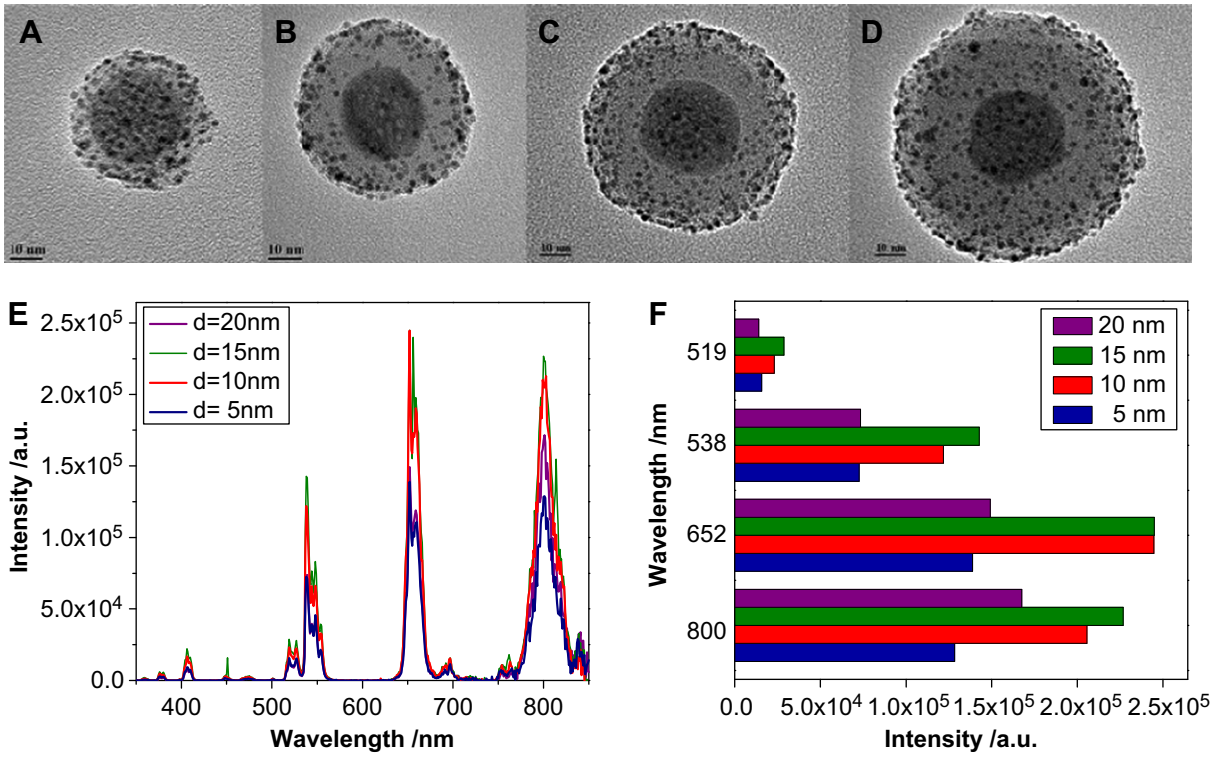

Fig. 5. (A–D) TEM images of UCS-Balls of different silica shell thicknesses: 5, 10, 15 and 20 nm (from left to right); (E, F) Emission spectra of UCS-Balls of different silica thicknesses and corresponding emission intensities at different wavelengths, excited by 980 nm laser (laser power = 261 mW, Y = 14 μg/mL).

UCNP ratios, from 0 to 1.187, were synthesized through changing the ratio between Au and UCNP (Fig. 6A–E). Efforts for even higher Au/UCNP ratios were not successful subjected to the limited density of NH_2-groups on the silica surface. As shown in Fig. 6F–G, after the decoration with Au NPs, the UCNP intensity became much stronger than the one without Au NPs. Especially at Au/Y = 0.274, fluorescence of UCS-Balls was almost 3–4 times stronger than that of UCNP@SiO_2. Under the presence of Au NPs, the local electromagnetic field around UCS-Balls will be enhanced, therefore the SPR effect might be predominant while the quenching effect of UCNP was neglectable at relatively low Au content of the Au/Y ratio = 0.274. The donor quenching efficiency E can be calculated according to the following Eq. (1) [49].

$$E = \frac{Nk_{et}(R)}{k_r + k_{nr} + Nk_{et}(R)} = \frac{1}{1 + \left(\frac{k_r + k_{nr}}{Nk_{et}(R)}\right)} \quad (1)$$

Where N is the number of Au NPs per one donator, R is the center-to-center separation distance, k_{et} is the energy transfer rate for single donor-acceptor pair, k_r and k_{nr} are the donor radiative and non-radiative rate, respectively. From the Eq. (1), the donor quenching efficiency E increased at the increased Au content (N). Therefore, when the Au/Y ratio increased to 0.539, the PL decreased remarkably as the quenching efficiency might increase much more quickly than the field enhancement. As the field enhancement and non-radiative quenching are the competitive processes with each other, Au could either enhance or decrease the PL intensity. The PL enhancement factor F can be presented in Eq. (2) [48].

$$F = f_a \times \frac{Q^*}{Q} = \frac{\sigma^*}{\sigma} \times \frac{Q^*}{Q} \quad (2)$$

Where f_a is a factor for the changes of field applied to the UCNPs, σ and σ* are UCNPs' absorption cross-sections without and with the proximal Au, respectively.

Q and Q* are Quantum Yields of the reference UCNPs sample and UCS-Balls, respectively. When more Au NPs were decorated outside, the absorption cross-sections (σ*), and also the enhancement factor F could become larger. As the Au/Y ratio further increased to 0.854 or 1.187, both quenching efficiency E and enhancement factor F could increase. As a result of competition between the two factors, the SPR effect became more significant than the quenching effect in the present case due to the strong local electromagnetic field enhancement at high Au contents. Unlike Huang's report on the significant emission intensity enhancement at increased number of attached Au NPs [45], we found a critical point at Au/Y = 0.539, below which fluorescence enhancement could be obtained. The UCNP in this study was only 25 nm in diameter, much smaller than that in Huang's report (*ca.* 180 nm), so the luminescence became weaker due to the strong PL quenching by numerous Au NPs attached on the outside surface of UCNP@SiO_2 nanostructure.

3.3. Cytotoxicity assay of UCS-Balls

To evaluate the potential application of UCS-Balls as imaging probes, its cytotoxicity should be checked at first. The cytotoxicity was assessed against MCF-7 cells using a typical MTT (3-(4, 5-dimethylthiazol-2-y1)-2, 5-diphenyltetrazolium bromide) cell viability assay. As shown in Fig. 7, more than 91.7% of the cells survived after the co-incubation with 800 μg/mL UCS-Balls for 6 h. As the co-incubation prolonged to 24 h, more than 85.3% of the cells survived, indicating a relatively low cytotoxicity of as-synthesized UCS-Balls.

3.4. Feasibility assessment of UCS-Balls in fluorescent imaging in vitro and in vivo

Cellular uptake of UCS-Balls was investigated (Fig. 8 and Fig. S3) using an Olympus FV1000 laser-scanning confocal microscope (LSCM) equipped with a continuous-wave (CW) NIR laser (λ = 980 nm,

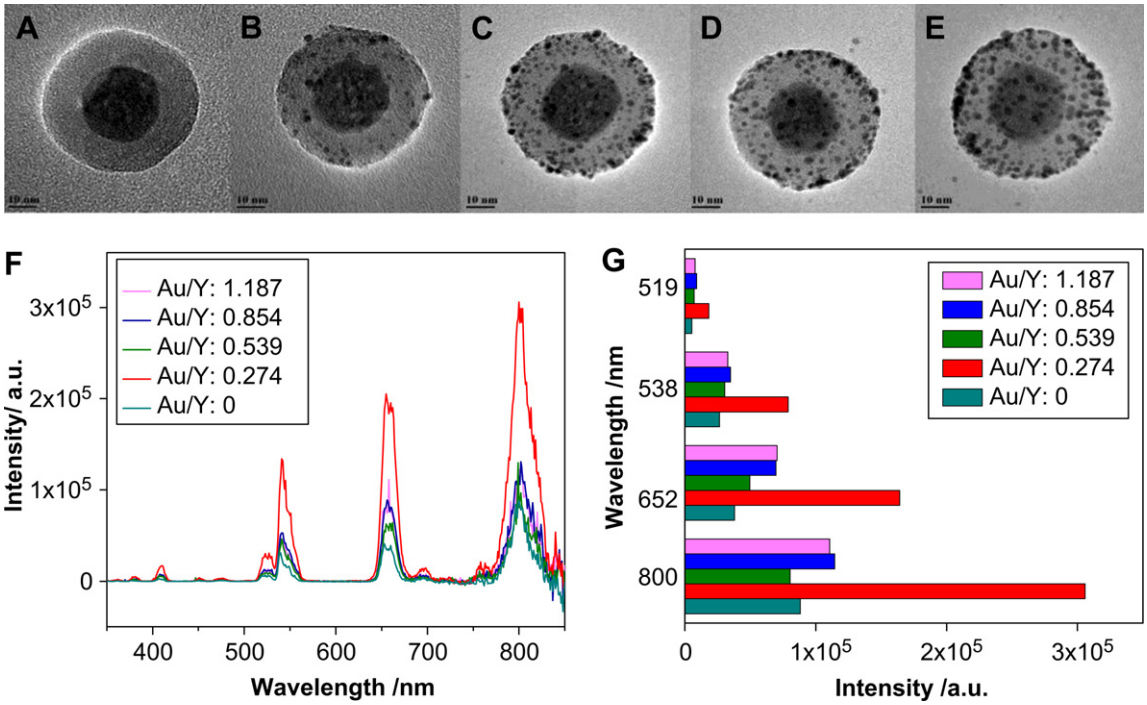

Fig. 6. (A–E) TEM images of UCS-Balls of different Au/Y molar ratios: 0, 0.274, 0.539, 0.854 and 1.187 (from left to right); (F, G) Emission spectra of UCS-Balls of different Au/Y molar ratios and corresponding emission intensities at different wavelengths, excited by 980 nm laser (laser power = 314 mW, Y = 10 μg/mL).

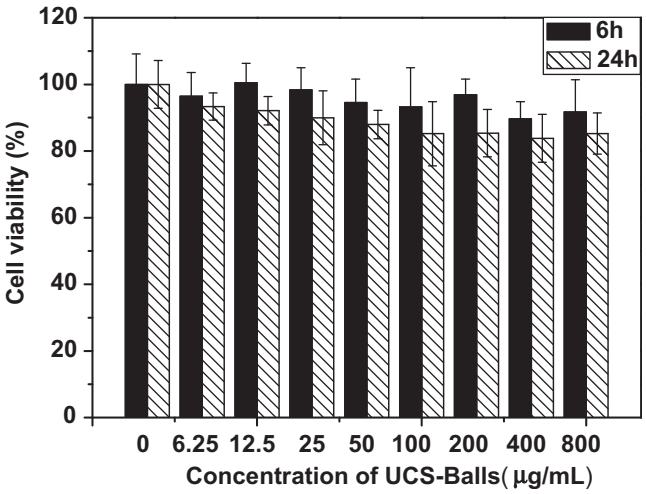

Fig. 7. *In vitro* cell viabilities of MCF-7 cells incubated with UCS-Balls of different concentrations (0, 6.25, 12.5, 25, 50, 100, 200, 400 and 800 μg/mL) for 6 h and 24 h.

power = 400 mW). As UCS-Balls have a wide wavelength range of emission, fluorescent of green and red emissions could be obtained under 980 nm laser excitation in the wavelength ranges of 500–560 nm and 620–680 nm, respectively. All images were taken under the identical conditions and the cell nucleus was stained blue with DAPI. From the confocal luminescence imaging of MCF-7 cells, the UCS-Balls have crossed the cell membrane and entered the cytoplasm. With both prolonging incubation time and increasing concentration of UCS-Balls, stronger fluorescence emissions without any cell auto-fluorescence can be observed (Figs. 8 and 9 at the top, S3), which show that the cellular uptake of NPs was both time- and dose-dependent, demonstrating that UCS-Balls are promising candidates for cellular labeling and imaging. To testify the suitability of UCS-Ball as an optical imaging probe *in vivo*, we subcutaneously injected the probe into a tumor borne in a mouse, and imaged the tumor using 980 nm laser (Fig. 10 at the top) at a dose of 303.2 μg Gd/kg (equal to 1.087 mg Au/kg). After the injection of UCS-Balls, the tumor emitted strong visible light under excitation of NIR laser, without any tissue auto-fluorescence observed, demonstrating that UCS-Balls were able to act as visible optical imaging probes *in vivo* as well.

3.5. Feasibility assessment of UCS-Balls in MRI in vitro and in vivo

Gadolinium (Gd^{3+})-based complexes have been widely used as efficient T_1-weighted MR contrast agents [60,61]. Owing to Gd^{3+} ions codoping, UCS-Balls are expected to shorten the T_1 (spin-lattice relaxation) time of water protons and act as a T_1-weighted MRI contrast agent [33,35]. As the concentration of Gd^{3+} increased, T_1-relaxation time of water protons was shortened significantly from 3597 ms to 1491 ms and T_1-weighted images became brighter (Fig. S4A). The influence of Au NPs in UCS-Ball on the specific relaxivity values (r_1) was also investigated here (Fig. S4B). With the addition of Au NPs (Au/Y = 0.854), r_1 value decreased from 1.70 to

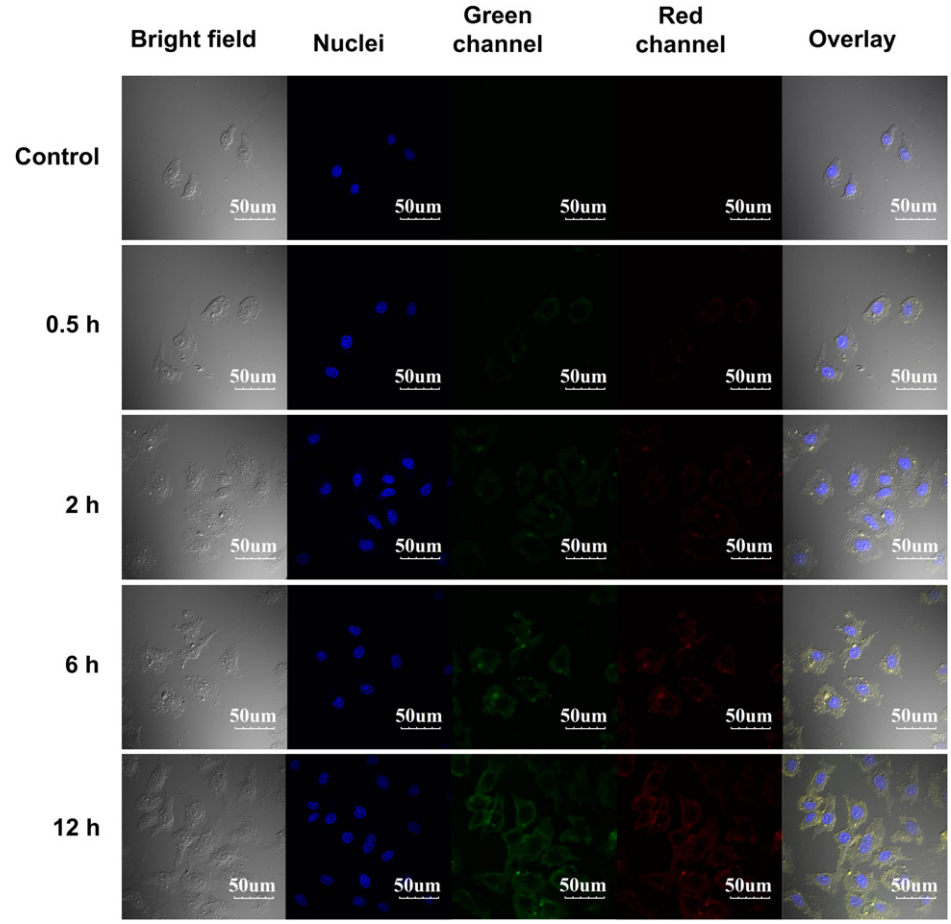

Fig. 8. Confocal fluorescence imaging of MCF-7 cells incubated with UCS-Balls at 800 μg/mL for different time periods of 0.5h, 2 h, 6 h and 12 h.

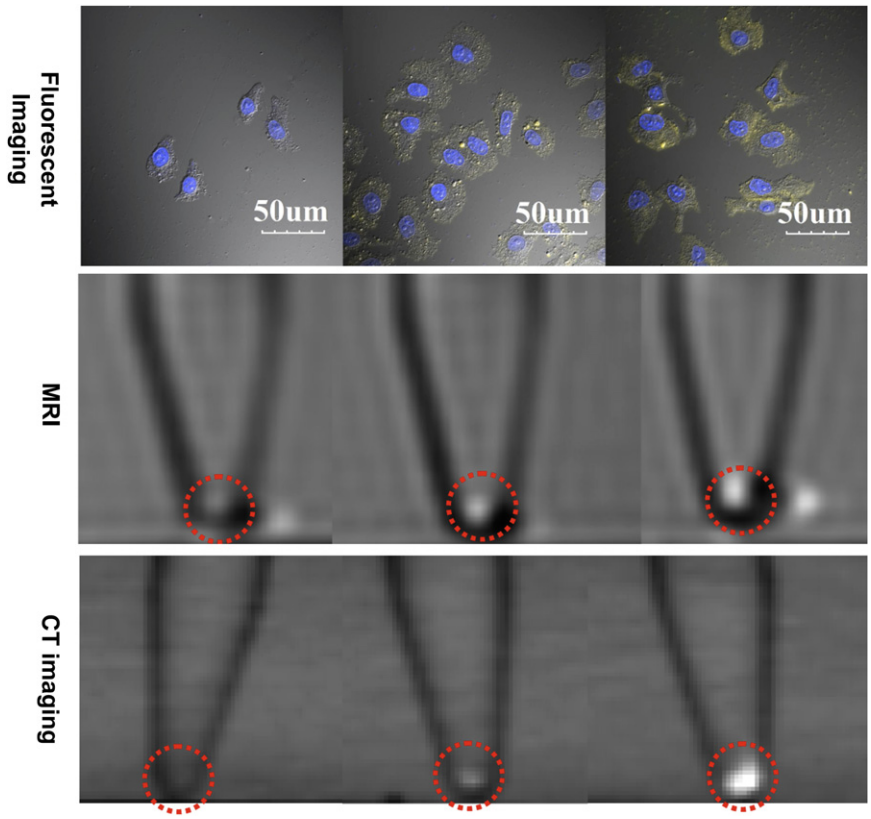

Fig. 9. Trimodal imaging demonstration of human breast cancer cell line (MCF-7) incubated with UCS-Balls for 12 h at various concentrations (from left to right): 0, 400 and 800 μg/mL. At the top: Confocal fluorescence imaging; In the middle: T_1-weighted MRI; At the bottom: CT imaging (HU value: 25.50, 90.75 and 250.50).

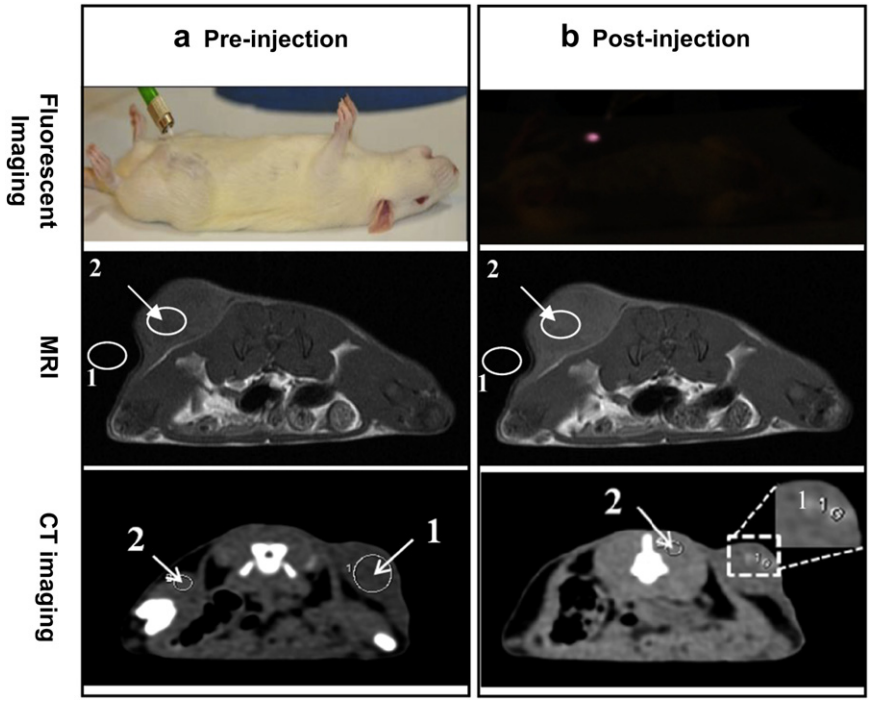

Fig. 10. Trimodal images of mice bearing a Walker 256 tumor using UCS-Balls: pre-injection (left), post-injection (right). At the top: pre- and post-injection fluorescence imaging using NIR laser (λ = 980 nm); In the middle: pre- and post-injection MR imaging; At the bottom: pre- and post-injection CT imaging. In MRI, area-1 and area-2 are for the background and tumor site, respectively, the SNR (signal intensity ratio of area-2/area-1) increased from 19.28 to 32.12 after local-injection of UCS-Balls (dose: 303.2 μg Gd/kg) at the tumor site. In CT imaging, area-1 and area-2 are for the tumor and soft tissue sites, respectively, and their HU value of tumor increased from 40.86 ± 5.66 to 102.34 ± 9.37 after local-injection of UCS-Balls (dose: 1.087 mg Au/kg) at the tumor site.

1.25 mM^{-1} s^{-1}, possibly due to the slightly reduced water accessibility by the decoration of Au NPs over UCNP@SiO_2.

In vitro T_1-weighted MRI of MCF-7 cells incubated with different concentrations (0, 400 and 800 μg/mL) of UCS-Balls (Au/Y = 0.854) was also investigated. After co-incubation for 12 h, the UCS-Balls not uptaken by the cells were washed away with PBS buffer. After centrifugation, cells bearing UCS-Balls were precipitated at the bottom of the tubes. As shown at the bottom of tubes in Fig. 9 (in the middle), T_1 images became brighter at higher concentrations of UCS-Balls, suggesting that UCS-Balls in cells could also affect the spin-lattice relaxation time *in vitro*. *In vivo* T_1-weighted MRI was conducted on a tumor-bearing mouse using a 3.0 T human MRI scanner and the images were shown in Fig. 10 (in the middle) and Fig. S5. Before injection, the SNR (signal intensity ratio of area-2 (tumor)/area-1 (background)) was 19.28. After local-injection of UCS-Balls at the tumor site (dose: 303.2 μg Gd/kg, 1.087 mg Au/kg), the SNR increased to 32.12 with an increased SNR of 66.6% due to the injection of UCS-Balls, which demonstrated the feasibility of UCS-Balls as MRI contrast agents *in vivo*.

3.6. Feasibility assessment of UCS-Balls in CT imaging in vitro and in vivo

With higher attenuation of X-ray than iodine, Au NPs have been recommended as a promising CT contrast agent [62–64]. Herein, *in vitro* CT imaging of MCF-7 cells incubated with different concentrations of UCS-Balls (Au/Y = 0.854) was also investigated. After the co-incubation for 12 h, the UCS-Balls not uptaken by the cells were washed away with PBS buffer. These cells after incubation with different UCS-Balls concentrations of 0, 400 and 800 μg/mL (with Au contents estimated to be 0, 50.4 and 100.8 μg/mL) and centrifugal precipitation were imaged using a clinical CT scanner and their HU values at the tube bottoms were found to be 25.50, 90.75 and 250.50, respectively (Fig. 9 at the bottom). The feasibility of UCS-Balls as CT contrast agents *in vivo* was also demonstrated by subcutaneously injecting the probes into the tumor. Pre-injection CT-image was shown in Fig. 10 (at the bottom, left) and Fig. S6A, area-1 was the tumor site and its HU value was estimated to be 40.86 ± 5.66, while the value of the soft tissue site (area-2) was 65.33 ± 3.69. After the injection of UCS-Balls (dose: 303.2 μg Gd/kg, 1.087 mg Au/kg), the HU value of the tumor site (area-1 in Fig. 10 at the bottom (right) and Fig. S6B) increased to 102.34 ± 9.37, while that of the soft tissue site (area-2) remained almost unchanged (61.00 ± 4.07). These differences in HU values in both *in vitro* and *in vivo* experiments suggested that UCS-Balls might be a promising contrast agent for CT imaging.

4. Conclusion

Sub-50 nm multifunctional nanoprobes (NaY/GdF_4: Yb, Er, Tm @SiO_2–Au) have been successfully constructed, which show monosized distribution, excellent dispersity in PBS buffer and low cytotoxicity. The effect of the distance between UCNP and Au NPs on the luminescence of UCNP was investigated and an optimal value of 10–15 nm was determined for strong fluorescence. Utilizing the SPR effect of Au NPs, the upconversion luminescence was further enhanced by 3–4 times at a Au/Y molar ratio of 0.274. The cellular uptake of UCS-Balls was found to be efficient, and time- and dose-dependent. Upconversion fluorescent imaging was demonstrated by the strong visible light emission under excitation of NIR laser without any auto-fluorescence both *in vitro* and *in vivo*. The feasibilities of UCS-Balls for MR and CT imaging were clearly evidenced by the intensified signals from UCS-Balls *in vitro* and the increased SNR of tumors after the local-injection of the nanoprobes *in vivo*.

Acknowledgements

This work was financially supported by the National Natural Science Foundation of China Research (Grant No. 50823007, 50972154, 51072212, 51102259), the Science and Technology Commission of Shanghai (Grant No. 10430712800, 10QH1402800). We thank Jianan Liu, Yu Chen, Yan Zhu, Qingfeng Xiao, Jingwei Feng, Linlin Zhang and YanYang from Shanghai Institute of Ceramics Chinese Academy of Sciences for useful discussions.

Appendix. Supplementary material

Supplementary material associated with this article can be found, in the online version, at doi:10.1016/j.biomaterials.2011.10.039.

References

[1] Kobayashi H, Ogawa M, Alford R, Choyke PL, Urano Y. New strategies for fluorescent probe design in medical diagnostic imaging. Chem Rev 2010;110:2620–40.
[2] Gunasekera UA, Pankhurst QA, Douek M. Imaging applications of nanotechnology in cancer. Targ Oncol 2009;4:169–81.
[3] Hallouard F, Anton N, Choquet P, Constantinesco A, Vandamme T. Iodinated blood pool contrast media for preclinical x-ray imaging applications - a review. Biomaterials 2010;31:6249–68.
[4] Cai W, Chen X. Nanoplatforms for targeted molecular imaging in living subjects. Small 2007;3:1840–54.
[5] Cheon J, Lee J- H. Synergistically integrated nanoparticles as multimodal probes for nanobiotechnology. Acc Chem Res 2008;41:1630–40.
[6] Wang X, Yang L, Chen Z, Shin DM. Application of nanotechnology in cancer therapy and imaging. Ca-cancer J Clin 2008;58:97–110.
[7] Louie AY. Multimodality imaging probes: design and challenges. Chem Rev 2010;110:3146–95.
[8] Hamoudeh M, Kamleh MA, Diab R, Fessi H. Radionuclides delivery systems for nuclear imaging and radiotherapy of cancer. Adv Drug Deliver Rev 2008;60:1329–46.
[9] Haller C, Hizoh I. The cytotoxicity of iodinated radiocontrast agents on renal cells in vitro. Invest Radiol 2004;39:149–54.
[10] Rabin O, Manuel Perez J, Grimm J, Wojtkiewicz G, Weissleder R. An x-ray computed tomography imaging agent based on long-circulating bismuth sulphide nanoparticles. Nat Mater 2006;5:118–22.
[11] Geso M. Gold nanoparticles: a new X-ray contrast agent. Brit J Radiol 2007;80:64–5.
[12] Wang H, Zheng L, Peng C, Guo R, Shen M, Shi X, et al. Computed tomography imaging of cancer cells using acetylated dendrimer-entrapped gold nanoparticles. Biomaterials 2011;32:2979–88.
[13] Oh MH, Lee N, Kim H, Park SP, Piao Y, Lee J, et al. Large-scale synthesis of bioinert tantalum oxide nanoparticles for x-ray computed tomography imaging and bimodal image-guided sentinel lymph node mapping. J Am Chem Soc 2011;133:5508–15.
[14] http://physics.nist.gov/PhysRefData/XrayMassCoef/.
[15] Talley CE, Jackson JB, Oubre C, Grady NK, Hollars CW, Lane SM, et al. Surface-enhanced raman scattering from individual Au nanoparticles and nanoparticle dimer substrates. Nano Lett 2005;5:1569–74.
[16] Zhang J, Noguez C. Plasmonic optical properties and applications of metal nanostructures. Plasmonics 2008;3:127–50.
[17] Haridas M, Tripathi LN, Basu JK. Photoluminescence enhancement and quenching in metal-semiconductor quantum dot hybrid arrays. Appl Phys Lett 2011;98:063305(1)–063305 (3).
[18] Roux S, Alric C, Taleb J, Le Duc G, Mandon C, Billotey C, et al. Gadolinium chelate coated gold nanoparticles as contrast agents for both x-ray computed tomography and magnetic resonance imaging. J Am Chem Soc 2008;130:5908–15.
[19] Shieh DB, Chou SW, Shau YH, Wu PC, Yang YS, Chen CC. In vitro and in vivo studies of FePt nanoparticles for dual modal CT/MRI molecular imaging. J Am Chem Soc 2010;132:13270–8.
[20] Michaelis J, Hettich C, Mlynek J, Sandoghdar V. Optical microscopy using a single-molecule light source. Nature 2000;405:325–8.
[21] Santra S, Yang H, Holloway PH, Stanley JT, Mericle RA. Synthesis of water-dispersible fluorescent, radio-opaque, and paramagnetic CdS: Mn/ZnS quantum dots: a multifunctional probe for bioimaging. J Am Chem Soc 2005;127:1656–7.
[22] Derfus AM, Chan WCW, Bhatia SN. Probing the cytotoxicity of semiconductor quantum dots. Nano Lett 2003;4:11–8.
[23] Kirchner C, Liedl T, Kudera S, Pellegrino T, Muñoz Javier A, Gaub HE, et al. Cytotoxicity of colloidal CdSe and CdSe/ZnS nanoparticles. Nano Lett 2004;5:331–8.
[24] Wang F, Liu X. Recent advances in the chemistry of lanthanide-doped upconversion nanocrystals. Chem Soc Rev 2009;38:976–89.

[25] Shen J, Sun L, Yan C. Luminescent rare earth nanomaterials for bioprobe applications. Dalton Trans; 2008:5687–97.
[26] Kramer KW, Biner D, Frei G, Gudel HU, Hehlen MP, Luthi SR. Hexagonal sodium yttrium fluoride based green and blue emitting upconversion phosphors. Chem Mater 2004;16:1244–51.
[27] Chen F, Zhang S, Bu W, Liu X, Chen Y, He Q, et al. A "neck-formation" strategy for an antiquenching magnetic/upconversion fluorescent bimodal cancer probe. Chem Eur J 2010;16:11254–60.
[28] Xia A, Gao Y, Zhou J, Li C, Yang T, Wu D, et al. Core-shell $NaYF_4$:Yb^{3+}, Tm^{3+}@Fe_xO_y nanocrystals for dual-modality T_2-enhanced magnetic resonance and NIR-to-NIR upconversion luminescent imaging of small-animal lymphatic node. Biomaterials 2011;32:7200–8.
[29] Hifumi H, Yamaoka S, Tanimoto A, Citterio D, Suzuki K. Gadolinium-based hybrid nanoparticles as a positive MR contrast agent. J Am Chem Soc 2006; 128:15090–1.
[30] Tsai CP, Hung Y, Chou YH, Huang DM, Hsiao JK, Chang C, et al. High-contrast paramagnetic fluorescent mesoporous silica nanorods as a multifunctional cell-imaging probe. Small 2008;4:186–91.
[31] Cheon J, Choi JS, Lee JH, Shin TH, Song HT, Kim EY. Self-confirming "and" logic nanoparticles for fault-free MRI. J Am Chem Soc 2010;132:11015–7.
[32] Wang F, Han Y, Lim CS, Lu YH, Wang J, Xu J, et al. Simultaneous phase and size control of upconversion nanocrystals through lanthanide doping. Nature 2010;463:1061–5.
[33] Kumar R, Nyk M, Ohulchanskyy TY, Flask CA, Prasad PN. Combined optical and MR bioimaging using rare earth ion doped $NaYF_4$ nanocrystals. Adv Funct Mater 2009;19:853–9.
[34] Park II Y, Kim JH, Lee KT, Jeon KS, Bin Na H, Yu JH, et al. Nonblinking and nonbleaching upconverting nanoparticles as an optical imaging nanoprobe and T_1 magnetic resonance imaging contrast agent. Adv Mater 2009;21: 4467–71.
[35] Zhou J, Sun Y, Du X, Xiong L, Hu H, Li F. Dual-modality in vivo imaging using rare-earth nanocrystals with near-infrared to near-infrared (NIR-to-NIR) upconversion luminescence and magnetic resonance properties. Biomaterials 2010;31:3287–95.
[36] Liu Q, Sun Y, Li C, Zhou J, Li C, Yang T, et al. ^{18}F-labeled magnetic-upconversion nanophosphors via rare-earth cation-assisted ligand assembly. Acs Nano 2011;5:3146–57.
[37] Zhou J, Yu M, Sun Y, Zhang X, Zhu X, Wu Z, et al. Fluorine-18-labeled Gd^{3+}/Yb^{3+}/Er^{3+} co-doped $NaYF_4$ nanophosphors for multimodality PET/MR/UCL imaging. Biomaterials 2011;32:1148–56.
[38] Nyk M, Kumar R, Ohulchanskyy TY, Bergey EJ, Prasad PN. High contrast in vitro and in vivo photoluminescence bioimaging using near infrared to near infrared upconversion in Tm^{3+} and Yb^{3+} doped fluoride nanophosphors. Nano Lett 2008;8:3834–8.
[39] Xiong L, Yang T, Yang Y, Xu C, Li F. Long-term in vivo biodistribution imaging and toxicity of polyacrylic acid-coated upconversion nanophosphors. Biomaterials 2010;31:7078–85.
[40] Jalil RA, Zhang Y. Biocompatibility of silica coated $NaYF_4$ upconversion fluorescent nanocrystals. Biomaterials 2008;29:4122–8.
[41] Chen F, Bu W, Chen Y, Fan Y, He Q, Zhu M, et al. A sub-50-nm monosized superparamagnetic Fe_3O_4@SiO_2 T_2-weighted MRI contrast agent: highly reproducible synthesis of uniform single-loaded core-shell nanostructures. Chem Asian J 2009;4:1809–16.
[42] Hamidi M, Azadi A, Rafiei P. Pharmacokinetic consequences of pegylation. Drug Deliv 2006;13:399–409.
[43] Li S, Huang L. Nanoparticles evading the reticuloendothelial system: role of the supported bilayer. Biochim Biophys Acta 2009;1788:2259–66.
[44] He Q, Zhang J, Shi J, Zhu Z, Zhang L, Bu W, et al. The effect of PEGylation of mesoporous silica nanoparticles on nonspecific binding of serum proteins and cellular responses. Biomaterials 2010;31:1085–92.
[45] Zhang H, Li Y, Ivanov IA, Qu Y, Huang Y, Duan X. Plasmonic modulation of the upconversion fluorescence in $NaYF_4$:Yb/Tm hexaplate nanocrystals using gold nanoparticles or nanoshells. Angew Chem Int Edit 2010;49:2865–8.
[46] Schietinger S, Aichele T, Wang HQ, Nann T, Benson O. Plasmon-enhanced upconversion in single $NaYF_4$: Yb^{3+}/Er^{3+} codoped nanocrystals. Nano Lett 2010;10:134–8.
[47] Kulakovich O, Strekal N, Yaroshevich A, Maskevich S, Gaponenko S, Nabiev I, et al. Enhanced luminescence of CdSe quantum dots on gold colloids. Nano Lett 2002;2:1449–52.
[48] Liu NG, Prall BS, Klimov VI. Hybrid gold/silica/nanocrystal-quantum-dot superstructures: synthesis and analysis of semiconductor-metal interactions. J Am Chem Soc 2006;128:15362–3.
[49] Pons T, Medintz IL, Sapsford KE, Higashiya S, Grimes AF, English DS, et al. On the quenching of semiconductor quantum dot photoluminescence by proximal gold nanoparticles. Nano Lett 2007;7:3157–64.
[50] Li Z, Zhang Y. An efficient and user-friendly method for the synthesis of hexagonal-phase $NaYF_4$: Yb, Er/Tm nanocrystals with controllable shape and upconversion fluorescence. Nanotechnology 2008;19:345606–10.
[51] Duff DG, Baiker A, Edwards PP. A new hydrosol of gold clusters .1.formation and particle-size variation. Langmuir 1993;9:2301–9.
[52] Arriagada FJ, Osseo-Asare K. Synthesis of nanosize silica in a nonionic water-in-oil microemulsion: effects of the water/surfactant molar ratio and ammonia concentration. J Colloid Interf Sci 1999;211:210–20.
[53] Friedman M, Williams LD. Stoichiometry of formation of Ruhemann's purple in the ninhydrin reaction. Bioorg Chem 1974;3:267–80.
[54] Liao H, Hafner JH. Monitoring gold nanorod synthesis on surfaces. J Phys Chem B 2004;108:19276–80.
[55] Srivastava S, Santos A, Critchley K, Kim K-S, Podsiadlo P, Sun K, et al. Light-controlled self-assembly of semiconductor nanoparticles into twisted ribbons. Science 2010;327:1355–9.
[56] Galow TH, Boal AK, Rotello VM. A "building block" approach to mixed-colloid systems through electrostatic self-organization. Adv Mater 2000;12:576–9.
[57] Gryczynski I, Malicka J, Shen Y, Gryczynski Z, Lakowicz JR. Multiphoton excitation of fluorescence near metallic particles: enhanced and localized excitation. J Phys Chem B 2002;106:2191–5.
[58] Zhou H, Xu C, Sun W, Yan C. Clean and flexible modification strategy for carboxyl/aldehyde-functionalized upconversion nanoparticles and their optical applications. Adv Funct Mater 2009;19:3892–900.
[59] Li Z, Wang L, Wang Z, Liu X, Xiong Y. Modification of $NaYF_4$:Yb, Er@SiO_2 nanoparticles with gold nanocrystals for tunable green-to-red upconversion emissions. J Phys Chem C 2011;115:3291–6.
[60] Lauffer RB. Paramagnetic metal complexes as water proton relaxation agents for NMR imaging: theory and design. Chem Rev 1987;87:901–27.
[61] Caravan P, Ellison JJ, McMurry TJ, Lauffer RB. Gadolinium(III) chelates as MRI contrast agents: structure, dynamics, and applications. Chem Rev 1999;99: 2293–352.
[62] Hainfeld JF, Slatkin DN, Focella TM, Smilowitz HM. Gold nanoparticles: a new X-ray contrast agent. Brit J Radiol 2006;79:248–53.
[63] Kopelman R, Popovtzer R, Agrawal A, Kotov NA, Popovtzer A, Balter J, et al. Targeted gold nanoparticles enable molecular CT imaging of cancer. Nano Lett 2008;8:4593–6.
[64] Cormode DP, Roessl E, Thran A, Skajaa T, Gordon RE, Schlomka JP, et al. Atherosclerotic plaque composition: analysis with multicolor CT and targeted gold nanoparticles. Radiology 2010;256:774–82.